Modeling Cracks in Clay at the Nanoscale through Molecular Dynamics

Zhe Zhang[1] and Xiaoyu Song, Ph.D.[2]

[1]Ph.D. Student, Dept. of Civil and Coastal Engineering, Univ. of Florida
[2]Associate Professor, Dept. of Civil and Coastal Engineering, Univ. of Florida.
Email: xysong@ufl.edu

ABSTRACT

In the present work, we carry out molecular dynamics (MD) simulations to investigate mechanism of crack in a single clay sheet. Uniaxial tension is applied to clay sheet in a strain-controlled manner. Crack initiates from the center of clay sheet and extends along the direction perpendicular to the loading direction. Finally crack extends through the whole slab and clay sheet is fractured into two halves. Bond breaking is first observed in silicon-oxygen bond, and later occurs in aluminum-oxygen bond. Numerical results show that crack propagation in single clay sheet is primarily contributed from bond breaking in Al-Ob and Si-Ob bonds. We find that crack length increases almost linearly with tensile strain. Atomic stress is calculated for both tetrahedral layer and octahedral layer considering the layered inhomogeneity of clay crystal structure. Stress intensity factor and energy release rate are computed based on MD simulation and are comparable to experimental results.

INTRODUCTION

Clay cracking could trigger failure in dam, slope, and embankment (Menon and Song, 2022a and b). Despite decades of progress, the assessment of clay cracking mechanisms has not been fully understood, especially considering the inherent microscale layered structure of clay minerals. A great number of experimental studies have been conducted to investigate drying-wetting induced desiccation cracking in clay (Mitchell and Soga 2005). Cracks in clay could introduce preferential flow paths for fluids and increase hydraulic conductivity. The increase in hydraulic conductivity due to fracturing could affect the long-term performance of landfill clay liners (Likos et al., 2019). Mechanical fracture properties of clay have also been investigated through, for example, tensile fracture in mode I loading condition (Wang et al., 2007) by directly applying load on clay sample at the laboratory scale. Cracking in clay is a multiscale problem. However, few works have been done to investigate mechanism of crack propagation in clay platelet at the atomic scale (Likos et al., 2019). At the atomic scale, cracking processes involve breaking of individual bonds between the atoms. It is of great importance to have a systematic understanding of the link between the microstructure of cracked clay sheet and their macroscopic failure behaviors under external loads. For example, cracks in clay can be across clay sheets (i.e., cracking orthogonal to the 001 plane) or between clay sheets (i.e., cracking parallel to the 001 plane) under certain loading conditions. The cracking mechanism of a single clay platelet could be critical to interpret and characterize the cracking process in clay at the continuum scale. We focus on the microscopic cracking behavior in clay in this work. With dramatic improvements in high-performance computing, molecular dynamics (MD) simulations open new avenues in studying the nanoscale hydromechanical properties of clay (Song and Zhang 2018; Song and Wang 2019; Zhang and Song 2021; Song and Zhang 2022). In this paper, we use full-scale MD

simulation to investigate the mechanism of crack nucleation and propagation in a single clay sheet at the atomic scale.

CLAY MODEL AND FORCE FIELD

Molecular model. The cell parameters of pyrophyllite unit cell $Al_2[Si_4O_{10}](OH)_2$ are $a = 5.16$ Å, $b = 8.966$ Å, $c = 9.347$ Å, $\alpha = 91.18°$, $\beta = 100.46°$, and $\gamma = 89.64°$. The clay sheet is built from the $18 \times 10 \times 1$ supercell, with dimensions $92.88 \times 89.66 \times 9.347$Å^3. Figure 1 shows the molecular model of the clay sheet at equilibrium.

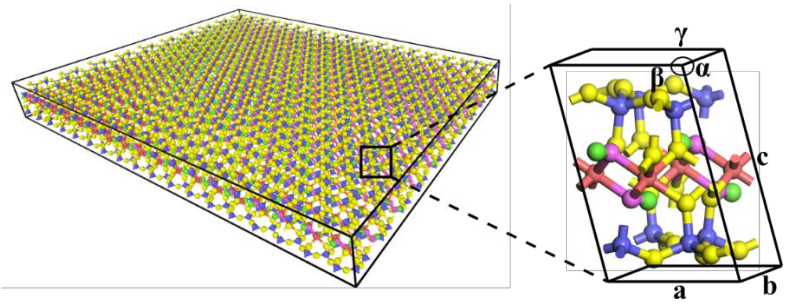

Figure 1. Molecular model of clay sheet.

Force field parameters. We employ ClayFF force field to represent interatomic interactions (Cygan et al., 2004). All ClayFF parameters are presented in Table 1. The nonbonded interaction between two atoms i and j is

$$E_{nonbonded} = \frac{q_i q_j}{4\pi\epsilon_0 r} + 4\epsilon_{ij}\left[\left(\frac{\sigma_{ij}}{r}\right)^{12} - \left(\frac{\sigma_{ij}}{r}\right)^{6}\right],$$

where q_i and q_j are atomic charges, ϵ_0 is the dielectric permittivity of vacuum, r is the distance between two atoms, ϵ_{ij} and σ_{ij} are empirical parameters calculated by the following mix rules:

$$\epsilon_{ij} = \sqrt{\epsilon_i \epsilon_j},$$

$$\sigma_{ij} = \frac{1}{2}(\sigma_i + \sigma_j).$$

Bond stretch and angle bend terms are taken from modified ClayFF (Pouvreau et al., 2017):

$$E_{Morse}^{bond} = D_0\left[1 - e^{-\alpha(r-r_0)}\right]^2,$$

$$E_{harmonic}^{angle} = k(\theta - \theta_0)^2.$$

In the Morse bond term, D_0 determines the depth of the potential wall, α is the stiffness parameter, and r_0 is the equilibrium bond length. In the harmonic angle term, k is the bending force constant, and θ_0 is the equilibrium angle.

Table 1. ClayFF parameters.

Nonbonded				
species	*symbol*	*q (e)*	*ϵ (kcal/mol)*	*σ (Å)*
Tetrahedral silicon	Si	2.1	1.8405×10^{-6}	3.7064
Octahedral aluminum	Al	1.575	1.3298×10^{-6}	4.7943
Bridging oxygen	Ob	−1.05	0.1554	3.5532
Hydroxyl oxygen	Oh	−0.95	0.1554	3.5532
Hydroxyl hydrogen	H	0.41	0	0

Bond stretch			
bond	D_0 *(kcal/mol)*	α *(Å^{-1})*	r_0 *(Å)*
Oh-H	132.2491	2.135	0.945

Angle bend		
Angle	*k (kcal mol^{-1} rad^{-2})*	θ_0 *(deg)*
Al-Oh-H	15	110

Simulations. MD simulations are performed on LAMMPS (Plimpton 1995) at $T = 298\,K$ using a time step of 1 fs. The pyrophyllite sheet is first relaxed during simulations in the NPT (constant number of atoms, constant pressure, and constant temperature) ensemble at zero pressure using the Nose-Hoover thermostat. The Verlet velocity algorithm is employed to integrate the equations of motion of atoms. Periodic boundary conditions are applied in all directions. Once the equilibrium state is obtained, we uniaxially stretch the periodic simulation box at a constant engineering rate to mimic the mode I tension condition. At each time step when the dimension of simulation box is changed, we remap atomic positions and force the clay particle to deform via an affine transformation that exactly matches the deformation of simulation box. The uniformly strain-controlled loading method is appropriate for MD simulations of solids (Plimpton 1995).

NUMERICAL RESULTS

In this section, we first examine the global stress-strain curves of clay sheet subject to mode I tension. Then we report the change in configurations of clay sheet during the complete crack process, i.e., from crack nucleation, and propagation, to final fracture. Having determined the critical bond length from the force-atomic distance relationship, we measure the number of broken bonds to further quantify crack process. The radial distribution function of different bond types is also calculated to describe microstructure change in clay. Stress intensity factor and energy release rate are calculated based on MD simulations and are compared to experimental results.

Stress-strain curve. We perform MD simulations of clay sheet under mode I tension with different strain rates. Figure 2 compares stress-strain curves at various strain rates ranging from $5e-8$ to $5e-5\,fs^{-1}$ and shows strong strain rate dependence. A larger strain rate yields higher ultimate strength at larger strain. We find stress-strain curves are almost identical below strain rate $1e-7\,fs^{-1}$. Thus, we assume $1e-7\,fs^{-1}$ as the critical strain rate and in what follows we present the numerical results of simulations performed at this strain rate. Figure 3 presents the corresponding force-displacement relation at strain rate $1e-7\,fs^{-1}$ during mode I

tension. The clay sheet deforms linearly before a displacement of 0.4 nm and then exhibits non-linearity. The maximum force is approximately 1.12×10^{-7} N at displacement 1.3 nm.

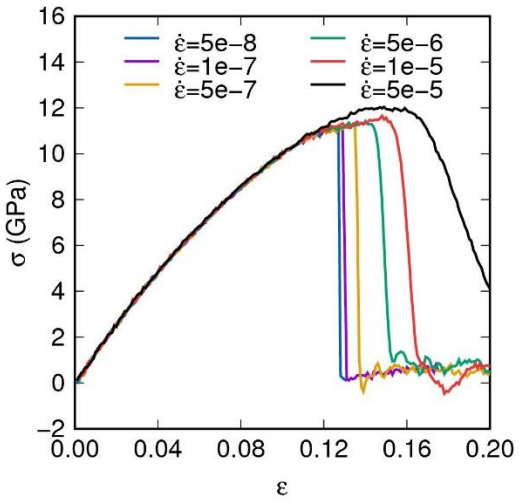

Figure 2. Stress-strain curves at different strain rates.

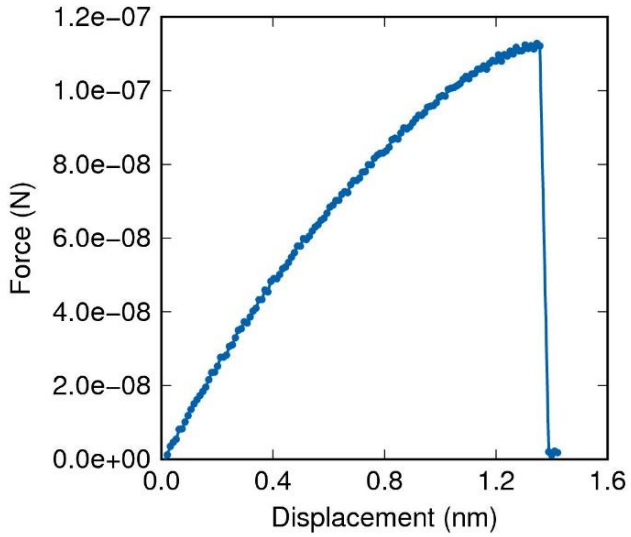

Figure 3. Load-displacement curve of clay sheet in mode I tension.

Crack nucleation and propagation. Figure 4 shows the process of crack nucleation and propagation in clay sheet. Crack initiates near the center of clay sheet at strain about 0.1226 and propagates along both positive and negative y-direction. Finally crack extends through the whole clay slab resulting in two halves. The increase in strain during crack process is less than 0.0002, indicating the brittle failure mode of clay sheet at the nanoscale.

Figure 5 plots the variation of crack length with tensile strain. Crack length is found to increase linearly with tensile strain and the final crack length is close to the y-dimension of clay sheet as expected.

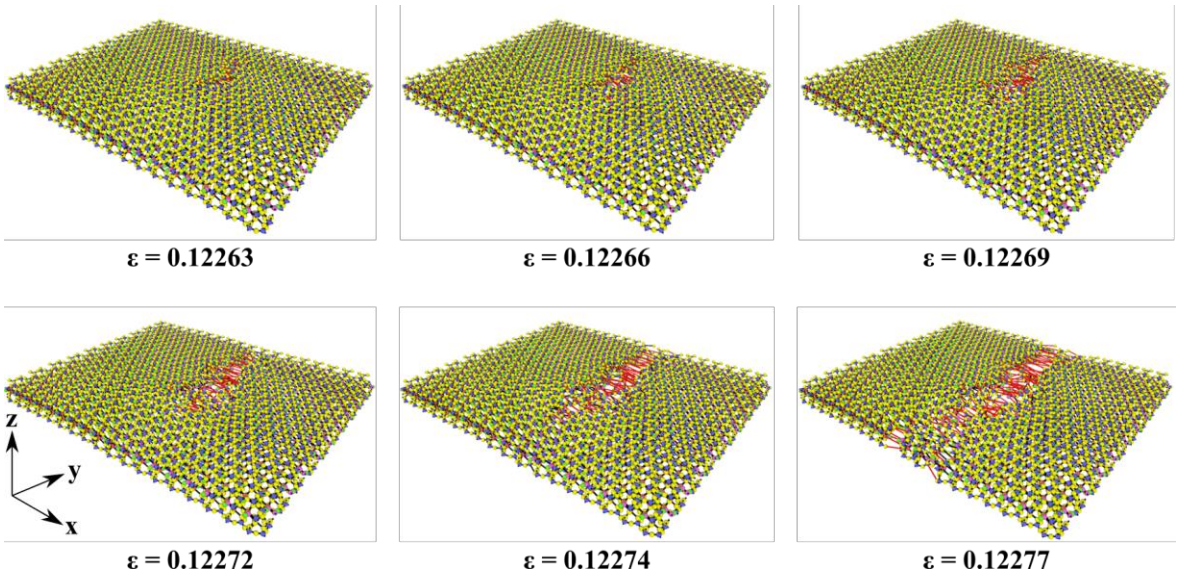

Figure 4. Crack process during tensile loading.

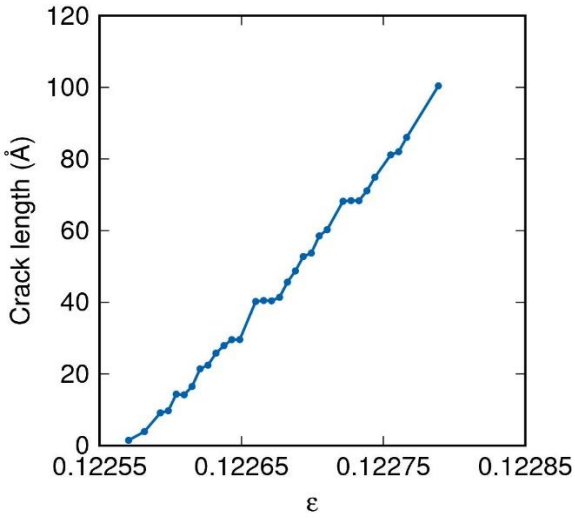

Figure 5. Crack process during tensile loading.

Atomic stress could help understand the mechanical response of clay at the nanoscale. Figure 6 shows the contour of atomic stress σ_{xx} in three layers in clay sheet: tetrahedral silicon layer, octahedral aluminum layer, and surface bridging oxygen layer. It is found atoms near the crack edge tend to have the minimum stress. For example, in the tetrahedral silicon layer and octahedral aluminum layer, the minimum σ_{xx} occurs near the inner boundary of crack region. In surface bridging oxygen layer, atomic stress tends to be zero for atoms near crack boundary.

Determination of critical bond length. Since ClayFF does not consider bond connectivity between metal-oxygen, we determine the critical bond length using potential energy and its derivative to atomic distance, i,e., atomic force. Figure 7 shows the magnitude of atomic interaction force as a function of distance. As the atomic distance approaches 5 Å, atomic forces between atom pairs Al-Oh, Al-Ob, and Si-Ob are close to zero. We assume at this distance the

atomic interactions are broken. Thus, 5 Å is determined as the critical bond length between metal and oxygen in this work.

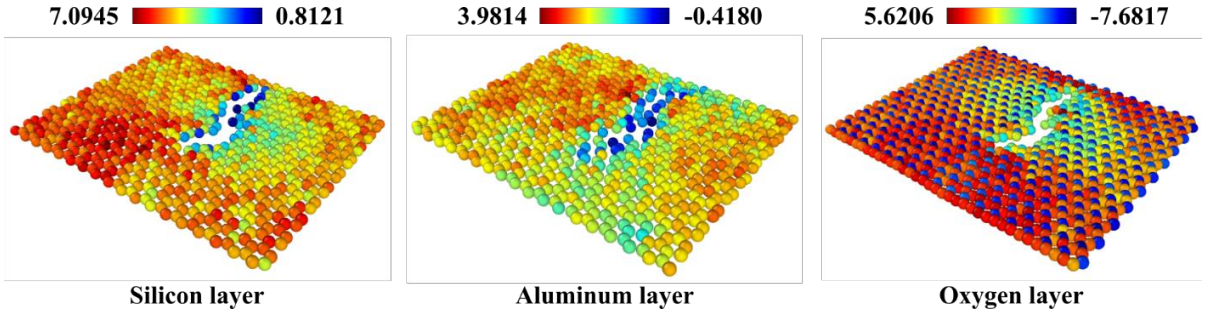

Figure 6. Contour of atomic stress at strain 0.1227 in different clay sublayers (unit: GPa).

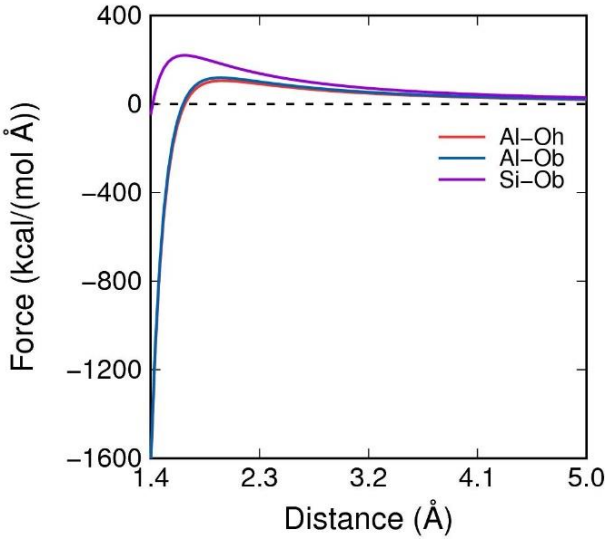

Figure 7. Atomic interaction force as a function of distance.

Bond breaking analysis. Figure 8 shows the number of broken bonds and the percentage of each type of broken bond during tensile loading. Bond breaking first occurs in Si-Ob bonds. Then Al-Oh type bond breaking can be seen after strain 0.1226. With further crack propagation, the percentage of broken bond numbers for each bond type gradually converges: 15.5% for Al-Oh, 44.2% for Al-Ob, and 40.3% for Si-Ob. We could speculate that crack propagation in single clay sheet is primarily contributed from bond breaking in Al-Ob and Si-Ob bonds.

We use the radial distribution function in terms of $g(r)$ to characterize the microstructure of clay and reflect the particle aggregation during deformation. $g_{\alpha\beta}(r)$ can be expressed as

$$g_{\alpha\beta}(r) = \frac{dN_\beta}{4\pi\rho_b r^2 dr},$$

where dN_β is the number of β atoms within the spherical bin of radius r and thickness dr enclosing an α atom at $r = 0$, and ρ_b is the number density of β atoms in the system.

Figures 9 shows the radial distribution function for three bond types at two different strain states. The peak value of $g(r)$ decreases after deformation for all bond types. The Si-Ob peak shifts right slightly which implies an increase in Si-Ob distance. However, the peak of Al-Ob and Al-Oh shifts left slightly.

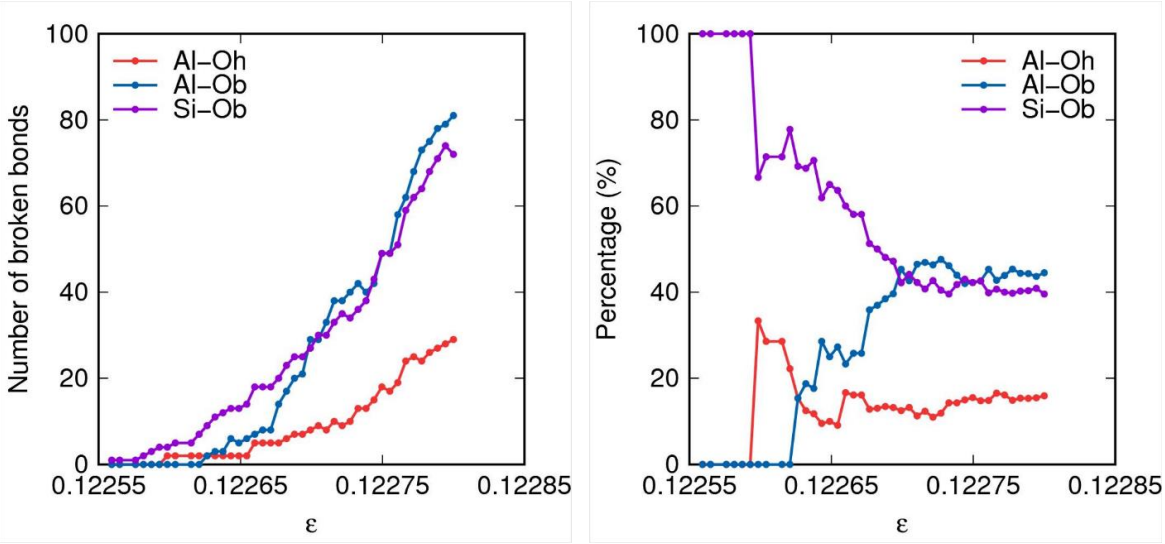

Figure 8. The number of broken bonds and percentage of broken bonds during clay crack.

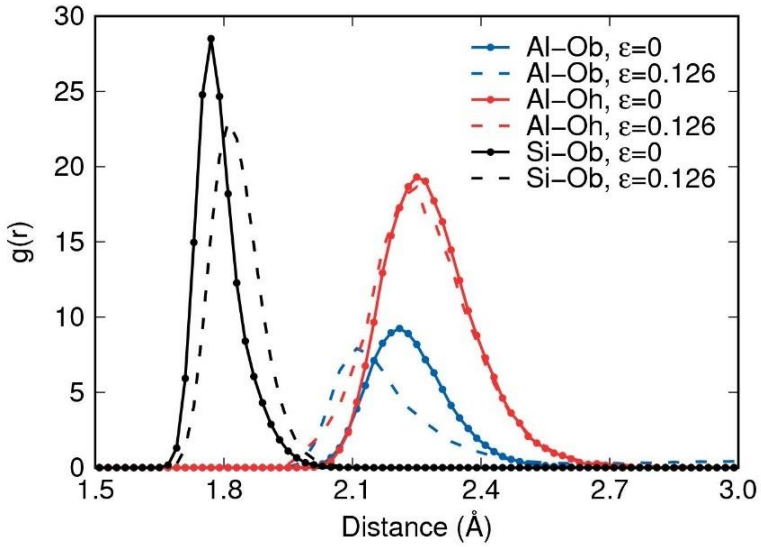

Figure 9. Radial distribution function of three bond types before and after tension.

MD-based fracture mechanics parameters.

In continuum fracture mechanics, the critical stress intensity factor (SIF) quantifies the resistance of a material to crack propagation. We estimate the microscale stress intensity factor based on atomistic fracture simulations. For Mode I tension, the SIF can be expressed as:

$$K_I = \sigma\sqrt{\pi a}\left[\frac{L_x}{\pi a}\tan\left(\frac{\pi a}{L_x}\right)\right]^{1/2},$$

where σ is the tensile stress, a is one half of crack length, L_x is the width of clay sheet. Figure 10 presents the variation of stress intensity factor with tensile strain. SIF increases upon loading and reaches the peak value 0.96 $MPa \cdot m^{1/2}$ at strain 0.12272. Spray (2010) reports that the fracture toughness of phyllosilicates mica is 0.2 $MPa \cdot m^{1/2}$.

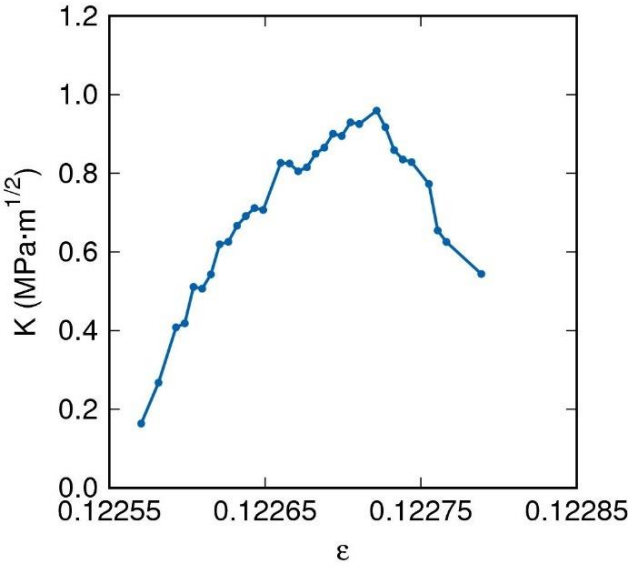

Figure 10. Stress intensity factor of the clay sheet during tensile loading.

Energy release rate G is defined as the dissipated energy during fracture per unit of newly created fracture surface area. Upon loading, the mechanical work provided to the system and stored in recoverable energy is released as crack propagates. The integration of stress σ with respect to strain ϵ provides an estimate of the variation of the free energy per unit volume. At the end of crack propagation, the mechanical energy has been completely released by crack surface creation. Under mode I condition, the integration of the stress-strain curve yields energy release rate G_I:

$$G_I = \frac{V}{2L_c t}\int_0^{\epsilon} \sigma d\epsilon,$$

where V is the system volume, and $L_c t$ is the simplified crack area expressed as the product of crack length L_c and thickness t. We multiply the crack area by 2 because the formation of a crack requires the creation of two surfaces, which means that surface area is twice the crack area. We calculate the energy release rate at the moment crack propagation is completed, $G_I = 6.1\ N/m$. The value is in the same order as the experimental results in Chandler (1984). The author used non-linear fracture mechanics and calculated the energy release rate of clay soil ranging from 4.3 to 6 N/m.

CONCLUSION

In this article, MD simulations were conducted on single clay sheet to understand the mechanism of crack propagation at the atomic scale. It is found: (i) Under mode I tension, crack initiates near the middle of clay sheet with silicon-oxygen bond breaking upon critical loading. (ii) Clay is fractured in a brittle manner at the nanoscale. Crack length increases linearly with tensile strain. The contour of atomic stress is plotted in tetrahedral layer and octahedral layer of clay incorporating its layered inhomogeneity. (iii) By calculating the number and percentage of broken bonds for each bond type, we speculate that crack propagation in single clay sheet is primarily contributed from bond breaking in Al-Ob and Si-Ob bonds. Through MD simulation we calculate fracture mechanics parameters stress intensity factor and energy release rate which are in the same order as experimental data.

REFERENCES

Chandler, H. W. (1984). "The use of non-linear fracture mechanics to study the fracture properties of soils." *J. Agric. Eng. Res.*, 29(4), 321-327.

Cygan, R. T., Liang, J. J., and Kalinichev, A. G. (2004). "Molecular models of hydroxide, oxyhydroxide, and clay phases and the development of a general force field." *J. Phys. Chem. B.*, 108(4), 1255-1266.

Houben, M. E., Desbois, G., and Urai, J. L. (2013). "Pore morphology and distribution in the Shaly facies of Opalinus Clay (Mont Terri, Switzerland): Insights from representative 2D BIB–SEM investigations on mm to nm scale." *Appl. Clay Sci.*, 71, 82-97.

Likos, W. J., Song, X., Xiao, M., Cerato, A., and Lu, N. (2019). "Fundamental challenges in unsaturated soil mechanics". In *Geotechnical fundamentals for addressing new world challenges* (pp. 209-236). Springer, Cham.

Mitchell, J. K., and Soga, K. (2005). *Fundamentals of soil behavior* (Vol. 3, p. USA). New York: John Wiley & Sons.

Menon, S., and Song, X. (2022a). "Computational coupled large-deformation peripоromechanics for dynamic failure and fracturing in variably saturated porous media." *Int. J. Numer. Methods Eng.* DOI: 10.1002/nme.7109.

Menon, S., and Song, X. (2022b). "Computational multiphase peripоromechanics for unguided cracking in unsaturated porous media." *Int. J. Numer. Methods Eng.*, 123(12), pp.2837-2871.

Plimpton, S. (1995). "Fast parallel algorithms for short-range molecular dynamics." *J. Comput. Phys.*, 117(1), 1-19.

Pouvreau, M., Greathouse, J. A., Cygan, R. T., and Kalinichev, A. G. (2017). "Structure of hydrated gibbsite and brucite edge surfaces: DFT results and further development of the ClayFF classical force field with metal-O-H angle bending terms." *J. Phys. Chem. C.*, 121(27), 14757-14771.

Song, X., Wang, M. C., and Zhang, K. (2018, January). "Molecular dynamics modeling of unsaturated clay-water systems at elevated temperature." In *The 7th International Conference on Unsaturated Soils 2018 (UNSAT2018)-Ng*, Leung, Chiu and Zhou, eds. The Hong Kong University of Science and Technology, ISBN 978-988-78037-3-7.

Song, X., and Wang, M. C. (2019). "Molecular dynamics modeling of a partially saturated clay-water system at finite temperature." *Int. J. Numer. Anal. Methods Geomech.*, 43(13), 2129-2146.

Song, X., and Zhang, Z. (2022). "Determination of clay-water contact angle via molecular dynamics and deep-learning enhanced methods." *Acta Geotech.*, 17(2), 511-525.
Spray, J. G. (2010). "Frictional melting processes in planetary materials: From hypervelocity impact to earthquakes." *Annu. Rev. Earth Planet. Sci.*, 38(1), 221-254.
Wang, J. J., Zhu, J. G., Chiu, C. F., and Zhang, H. (2007). "Experimental study on fracture toughness and tensile strength of a clay." *Eng. Geol.*, 94(1-2), 65-75.
Zhang, Z., and Song, X. (2021). "Characterizing the Impact of Temperature on Clay-Water Contact Angle in Geomaterials during Extreme Events by Deep Learning Enhanced Method." In *Geo-Extreme 2021* (160-168).
Zhang, Z., and Song, X. (2022). "Nonequilibrium molecular dynamics (NEMD) modeling of nanoscale hydrodynamics of clay-water system at elevated temperature." *Int. J. Numer. Anal. Methods Geomech.*, 46(5), 889-909.